JOURNAL OF MATERIALS SCIENCE **34** (1999) 1301–1311

Axial compression bending tests on carbon films and carbon fiber composites

M. SHIOYA*, M. NAKATANI, K. NAKAO
Department of Organic and Polymeric Materials, Tokyo Institute of Technology, 2-12-1 O-okayama, Meguro-ku, Tokyo 152, Japan
E-mail: mshioya@o.cc.titech.ac.jp

A. TAKAKU
Seitoku University, 531 Sagamidai, Matsudo-shi, Chiba 271, Japan

It is often desired to conveniently estimate the strength of materials by using specimens with small sizes. For this purpose, axial compression bending tests were examined by using carbon films and carbon fiber/epoxy resin unidirectional composite strands. The bending strength estimated from the axial displacement and the compression load coincided with the bending strength estimated from the deflection and the compression load. The carbon films showed specimen length dependence of the bending strength. The carbon fiber composite strand with a short specimen length produced a falling load compression curve. It was shown that the bending strength of the specimens showing falling load compression curves can be practically estimated by using the effective cross-section sizes at fracture. This analysis method is preferable also in order to minimize the error in the bending strength caused by the error in the cross-section size.

1. Introduction

In the studies for developing advanced materials, it is often desired to conveniently estimate mechanical properties of the materials by using specimens with small sizes. This requirement frequently arises in the studies of carbons prepared by pyrolysis since the size of the furnace for the heat-treatment impose the limitation on the size of the specimen and it is time consuming and costly to prepare a large amount of specimens with a larger size. For the conventional tensile tests, the specimen should be large enough to grip the specimen without slippage and fracture during the tests. On the other hand, for the bending tests by means of axial compression, there is no limitation on the size of the specimen with relation to the gripping problem.

The three- and four-point bending tests are widely used techniques to conveniently obtain the bending strength and the bending modulus. It has been pointed out, however, that these bending tests are insufficient for advanced composite materials because local fracture tends to occur at the loading points due to stress concentration [1]. In order to avoid this unfavorable stress concentration, specially designed loading zigs have been developed [2]. Fukuda proposed a method and a loading zig for the axial compression bending tests to overcome the disadvantages of the three- and the four-point bending tests [3]. The axial compression bending tests have been utilized to estimate the mechanical properties of the curved specimens of thermoplastic composites fabricated by filament winding [4].

In the present study, the axial compression bending tests are carried out on the specimens with small sizes without using a special loading zig. Carbon films and carbon fiber/epoxy resin unidirectional composite strands are tested with this method. The problems arising with this method are elucidated and an analysis method to overcome these problems is shown.

2. Theoretical

2.1. Axial compression bending of bar

Schematics of the axial compression bending test and the coordinate system used for analysis are shown in Fig. 1. A compression load, F, is applied to the bar, $O'R'$, with length, L, in the x direction without applying a bending moment at both ends of the bar. If the compression load is increased beyond a critical load, F_c, the bar buckles into a curve OQR. The curvature of the bar is given by $-\mathrm{d}\theta/\mathrm{d}s$ where s is the distance measured along the axis of the bar from the origin O and θ is the angle between the axis of the bar and x axis. The bending moment of the bar at a position (x, y) is Fy. Thus, by neglecting the changes in length of the bar due to compression, the following differential equation is obtained.

$$EI\frac{\mathrm{d}\theta}{\mathrm{d}s} = -Fy \tag{1}$$

where E is the bending modulus and I the moment of inertia of area. Since y is related to s by the equation,

$$\frac{\mathrm{d}y}{\mathrm{d}s} = \sin\theta \tag{2}$$

* To whom all correspondence should be addressed.

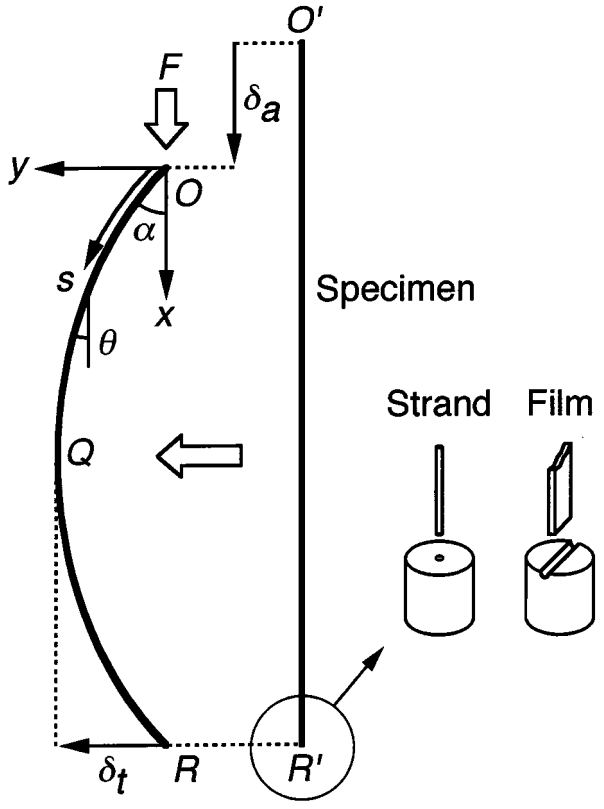

Figure 1 Schematic of axial compression bending test.

the differential equation takes a form,

$$\frac{\mathrm{d}^2\theta}{\mathrm{d}s^2} = -k^2 \sin\theta \tag{3}$$

where

$$k = \sqrt{\frac{F}{EI}} \tag{4}$$

The deflection curve obtained by solving the exact differential equation shown above is called the elastica, and the derivation is shown in a text book [5]. In the following, the results obtained by solving Equation 3 are shown briefly.

For the bar to buckle, the compression load F should be larger than a critical load F_c.

$$F \geq F_c = \frac{\pi^2 EI}{L^2} \tag{5}$$

The value of θ at the end of the bar, α, is determined in response to the compression load as follows:

$$kL = 2K(p) \tag{6}$$

$$p = \sin\frac{\alpha}{2} \tag{7}$$

where $K(p)$ is the complete elliptic integral of the first kind defined as

$$K(p) = \int_0^{\pi/2} \frac{1}{\sqrt{1 - p^2 \sin^2\phi}}\,\mathrm{d}\phi \tag{8}$$

Thus, the inclination angle α is determined from the values of E, I, L and F.

The deflection curve (x, y) and the distance s can be calculated as follows:

$$x = \frac{L}{K(p)} \int_\phi^{\pi/2} \left[\sqrt{1 - p^2 \sin^2\phi} - \frac{1}{2\sqrt{1 - p^2 \sin^2\phi}}\right] \mathrm{d}\phi \tag{9}$$

$$y = \frac{Lp}{K(p)} \cos\phi \tag{10}$$

$$s = \frac{L}{2} - \frac{L}{2K(p)} \int_0^\phi \frac{1}{\sqrt{1 - p^2 \sin^2\phi}}\,\mathrm{d}\phi \tag{11}$$

In these equations, the angle ϕ is defined as

$$\sin\frac{\theta}{2} = p \sin\phi \tag{12}$$

That is, ϕ varies continuously along the bar from 0 at the point Q to $\pi/2$ at the point O. Thus, by changing ϕ in the range from 0 to $\pi/2$ and calculating the values of x and y, the deflection curve QO is obtained. The deflection curve QR is symmetrical with the curve QO.

The parameters characterizing the deflection curve involve axial displacement, δ_a, deflection, δ_t and radius of curvature at point Q, r_o. These parameters are given as follows:

$$\frac{\delta_a}{L} = 2\left[1 - \frac{E(p)}{K(p)}\right] \tag{13}$$

$$\frac{\delta_t}{L} = \frac{p}{K(p)} \tag{14}$$

$$\frac{r_o}{L} = \frac{t}{(|\varepsilon_t| + |\varepsilon_c|)L} = \frac{1}{4pK(p)} \tag{15}$$

where t is the thickness of the bar in the y direction before bending, ε_t and ε_c are the strains at the convex and the concave sides of the bar at the point Q, and $E(p)$ is the complete elliptic integral of the second kind defined as

$$E(p) = \int_0^{\pi/2} \sqrt{1 - p^2 \sin^2\phi}\,\mathrm{d}\phi \tag{16}$$

It should be noted that for a given length L, the deflection curve and the parameters shown above are determined only by the inclination angle α.

The axial tensile and compressive stresses in the bar reach maximum at the convex and the concave sides of the bar at the point Q, respectively. The bar fractures when the maximum stress reaches either of the tensile or the compression strength of the bar, whichever is smaller. By denoting the compression load at fracture as F_b, the tensile or the compression strength, σ_b, is given by the equation

$$\sigma_b = \frac{t\delta_t F_b}{2I} \tag{17}$$

where δ_t here is the deflection at fracture. For a bar with a rectangular cross-section with thickness t and width b,

$$I = \frac{1}{12} bt^3 \tag{18}$$

For a bar with a circular cross-section with radius R,

$$t = 2R \tag{19}$$

and

$$I = \frac{\pi}{4} R^4 \tag{20}$$

Therefore, if any one of axial displacement, deflection, radius of curvature or inclination angle is measured at fracture, the deflection in Equation 17 is obtained directly or calculated by using Equations 13 to 15, and the tensile or the compression strength of the bar is estimated with the compression load at fracture. If the critical load can be measured, the modulus of the bar is estimated by using Equation 5.

2.2. Effective specimen length

For testing the specimens which show the length dependence of the strength, it is important to know the length of the specimen over which the tensile and compressive stresses are effectively imposed by the axial compression bending. Let us define the effective specimen length, s_o, as the length of the part of the specimen in which the axial stress exceeds a certain stress level. Then, the effective specimen length is estimated as follows: The axial stress, σ, at a distance z from the neutral plane in an arbitrary cross-section of the specimen is given by

$$\sigma = \frac{zyF}{I} \tag{21}$$

The stress σ reaches maximum in the central cross-section of the specimen since y reaches maximum. By defining β as the ratio of the stress σ in an arbitrary cross-section against the maximum stress at the same distance z in the central cross-section, the following equation is obtained from Equations 10 and 21.

$$\beta = \cos\phi \tag{22}$$

Thus, the effective specimen length where the axial stress exceeds β times maximum axial stress is given by the equation

$$s_o = L - 2s \tag{23}$$

where ϕ for calculating s is given by the inverse function of Equation 22. It can be shown that the effective specimen length at fracture is a function of β, $\sigma_b/(tE)$ and L.

The variation of the effective specimen length with the length of the specimen tested is shown in Fig. 2 for various values of $\sigma_b/(tE)$ and $\beta = 0.9$. It is known that when the specimen length is less than 50 mm, the effective specimen length varies almost in proportion to the length of the specimen tested.

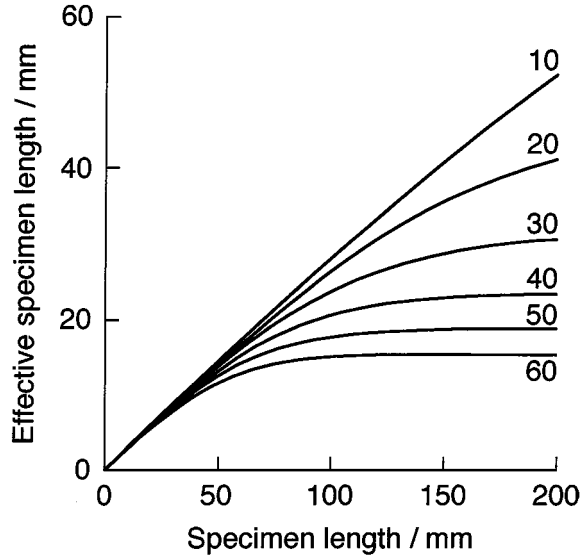

Figure 2 Effective specimen length, s_o, as a function of specimen length, L, for $\beta = 0.9$ and various values of $\sigma_b/(tE)$ shown in figure in units of m^{-1}.

2.3. Shear stress arising during axial compression bending

For the composite strands, the interfacial shear strength between the fiber and the matrix resin is usually much lower than the tensile or the compressive strength of the composite strands. Thus, it is worthwhile to know the values and the distribution of the shear stress arising during axial compression bending.

When the bar is bent by the axial compression load, not only normal stresses but also shear stresses are produced in a cross-section of the bar. In an arbitrary cross-section of the bar at a distance s from the end of the bar, an orthogonal coordinate system, z-w, is defined so that the z axis is included in the cross-section and the x-y plane as shown in Fig. 3. If the cross-section is symmetrical with respect to z-s plane, the tangents to the boundary of the cross-section at points U and V intersect at a point T on the z axis. The following two assumptions can be adopted for the shear stress, τ, in the cross-section. First, the shear stress at any point of the line UV is directed toward or away from the

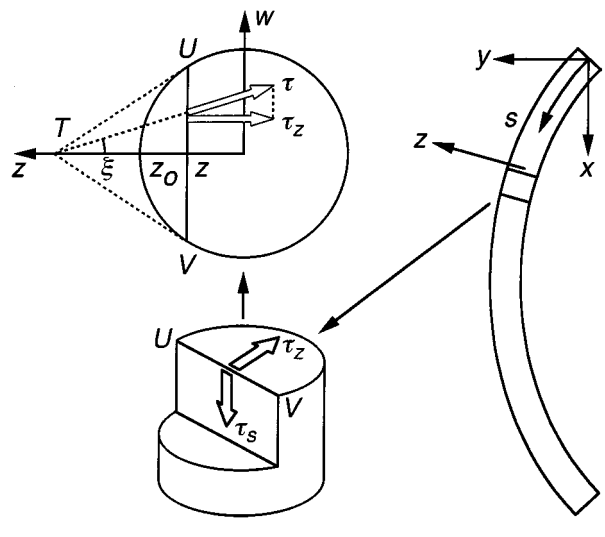

Figure 3 Shear stress produced during axial compression bending.

point T. Second, the components of the shear stresses parallel to the z axis, τ_z, are equal for all points of the line UV. It is known that the above two assumptions give satisfactory accuracy for practical application [6]. Then, the shear stress at a position (z, w) is given by the equation [6],

$$\tau = \frac{P}{I b(z) \cos \xi} \int_z^{z_0} b(z) z \, dz \tag{24}$$

where $b(z)$ is the length of the line UV and P is the shear force acting in the cross-section.

$$P = F \sin \theta \tag{25}$$

Thus, for a bar with a rectangular cross-section with thickness t and width b, the shear stress is given by

$$\tau = \frac{3}{2} \sigma_c \sin \theta \left[1 - \left(\frac{2z}{t} \right)^2 \right] \tag{26}$$

where

$$\sigma_c = \frac{F}{bt} \tag{27}$$

For a bar with a circular cross-section with radius R, the shear stress is given by

$$\tau = \frac{4}{3} \sigma_c \sin \theta \sqrt{\left(\frac{w}{R} \right)^2 \left(\frac{z}{R} \right)^2 + \left[1 - \left(\frac{z}{R} \right)^2 \right]^2} \tag{28}$$

where

$$\sigma_c = \frac{F}{\pi R^2} \tag{29}$$

It should be noted that the distribution profiles, in the z-s plane, of the shear stress normalized by the maximum value are the same for bars with rectangular and circular cross-sections since z-dependent terms in Equations 26 and 28 coincide at $w = 0$ and $R = t/2$.

The contour map, in the z-s plane, of the shear stress τ normalized by the maximum value is shown in Fig. 4. This distribution profile was calculated at the axial displacement of 0.08 times the length of the bar. The contour maps, in the z-w plane, of the shear stress τ normalized by the maximum value in this plane are also shown in Fig. 4 for rectangular and circular cross-sections.

When the shear stress acts in the cross-section perpendicular to the axis of the bar, a shear stress also arises in the cross-section parallel to the axis of the bar. It is known from the equilibrium of the moment due to shear forces that the shear stress τ_s in the longitudinal cross-section parallel to the neutral plane, which is directed parallel to the axis of the bar, has an equivalent intensity to the shear stress τ_z in the transverse cross-section. Since the shear stress τ_z equals τ where $\xi = 0$, the distribution of the shear stress τ_s in the z-s plane is the same as the distribution of the shear stress τ shown in the left side of Fig. 4. In actual axial compression bending tests, the shear force applied at the end of the bar is not uniformly distributed over the entire cross-section but rather concentrated on a contact point with the loading base. Thus, at the very end of the bar, the shear stress distribution may be disturbed. It is considered, however, that except for this limited region, the shear stress τ_s is distributed as shown in the left side of Fig. 4.

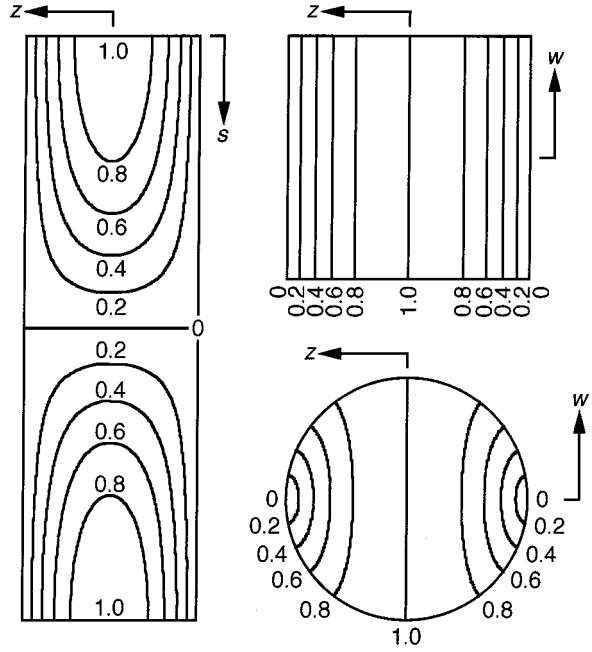

Figure 4 Contour maps, in z-s and z-w planes, of shear stresses, τ, arising in rectangular and circular cross-sections during axial compression bending. Contour map in z-s plane was calculated at axial displacement of 0.08 times length of bar. Values in figure show shear stresses normalized by maximum values in respective planes.

3. Experimental

3.1. Specimens

Polycarbodiimide(PCDI)-based carbon films [7, 8] are attractive materials in applications as the base-plates for information-recording hard-discs and the separators for fuel cells. The axial compression bending tests were carried out on the PCDI-based carbon films processed at temperatures from 600 to 2500 °C. The specimens were 10 mm long and 1 mm wide, and 50 mm long and 5 mm wide. The thicknesses of the specimens were 150 and 250 μm.

The axial compression bending tests were also carried out on carbon fiber/epoxy resin unidirectional composite strands. The fibers used were two types of polyacrylonitrile(PAN)-based carbon fibers denoted as T4 and H4 and a pitch-based carbon fiber, X5. These fibers were in the form of continuous filament yarn and the characteristics of these fibers are given in Table I. The compressive strength of the fibers determined with micro-compression tests on single-filaments [9] is also included in Table I. The epoxy resin used was a mixture of diglycidylether of bisphenol A-type epoxy resin, methylnadic acid anhydride, benzyldimethylamine and methyl ethyl ketone by the weight ratio of 100 : 90 : 2.5 : 15. A single fiber tow was soaked in liquid epoxy

TABLE I Characteristics of carbon fibers used for composite strands

Fiber	Filament number per tow	Diameter (μm)	Tensile strength[a] (GPa)	Compressive strength[b] (GPa)
T4	12000	6.81	4.9	2.0
H4	12000	6.42	4.4	1.6
X5	4000	10.1	3.6	0.51

[a]Estimated with tensile tests on 100 mm long composite strands by dividing fracture load with fiber cross-section area.
[b]Estimated with micro-compression tests on single-filaments [9].

resin, passed through a circular die to adjust fiber volume fraction, and wound on a frame. By leaving the resin impregnated fiber two at room temperature for 18 h, the methyl ethyl ketone was evaporated. Then, the resin impregnated fiber tow was cured in an air circulating oven at 110 °C for 2 h and additionally at 150 °C for 1 h. The composite strands prepared in this way had circular cross-sections.

3.2. Axial compression bending test

The axial compression bending tests were carried out by using a universal tester (Tensilon, Orientec). The specimen was axially compressed between two metal bases as shown in Fig. 1. The metal bases had a groove or a dimple for the tests of the films and the composite strands, respectively, in order to prevent recoiling of the specimen. The groove was 0.7 mm wide, 0.06 mm deep, and having an arced cross-section 1 mm in radius. The dimple was 1.2 mm in diameter, 0.2 mm deep, and having a spherical surface 1.0 mm in radius. The ends of the composite strands were ground into a hemispherical shape with sandpaper.

The deformation of the specimen was monitored by using a charge-coupled device camera from the normal direction to the bending. From the images of the specimen and a scale placed nearby, the deflection was measured. The axial displacement was calculated from the loading time and the crosshead speed. The crosshead speeds were 0.2 and 5 mm min^{-1} for the 10 and 50 mm long carbon films, respectively, and 0.5 mm min^{-1} for the composite strands.

3.3. Sonic modulus

The sonic propagation velocity of the specimen in free state was measured as follows [10]: First, the specimen was placed on a rubber board and a transmitter and a receiver made of piezotransducers were pressed on the specimen from above. Then, the time interval from the issuance of 1 MHz ultrasonic waves to reception was measured. From the changes in the time interval with the distance between the transmitter and the receiver, the sonic propagation velocity, C, was determined. The sonic modulus, E_s, was calculated by using the equation,

$$E_s = \rho C^2 \tag{30}$$

where ρ is the density of the specimen. The sonic modulus of carbon fiber unidirectional composite strands measured in free state coincides with the tensile modulus determined from the initial slope of the stress-strain curves [10].

3.4. Density and fiber volume fraction

The densities of carbon films, composite strands, carbon fibers and matrix resin plate which was cured with the same conditions as the composite strands were measured at 30 °C by a sink-float method using a *n*-heptane, carbon tetrachloride and ethylene dibromide mixture.

The fiber volume fraction, v_f, in the composite strand was calculated by using the equation,

$$\rho_c = v_f \rho_f + (1 - v_f)\rho_m \tag{31}$$

where ρ_c, ρ_f and ρ_m are the densities of the composite strand, carbon fiber and matrix resin.

4. Results and discussion

4.1. Compression curves

The compression curve representing load-axial displacement relation during the axial compression bending test on a PCDI-based carbon film 50 mm long, 150 μm thick and processed at 2200 °C is shown in Fig. 5. In this figure, the compression curve predicted from Equations 4, 6 and 13 with $EI = 3.80 \times 10^{-5}$ Nm^2 and $L = 50$ mm is also shown. The critical point at which pure compression changes into bending is not

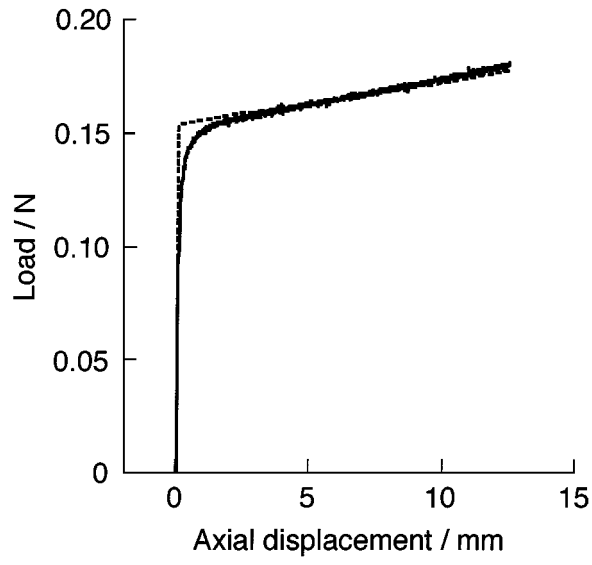

Figure 5 Load-axial displacement diagram of axial compression bending test on PCDI-based carbon film. Film is 50 mm long, 150 μm thick and processed at 2200 °C. Experimental result (-) and values calculated with $EI = 3.80 \times 10^{-5}$ Nm^2 and $L = 50$ mm (. . .) are shown.

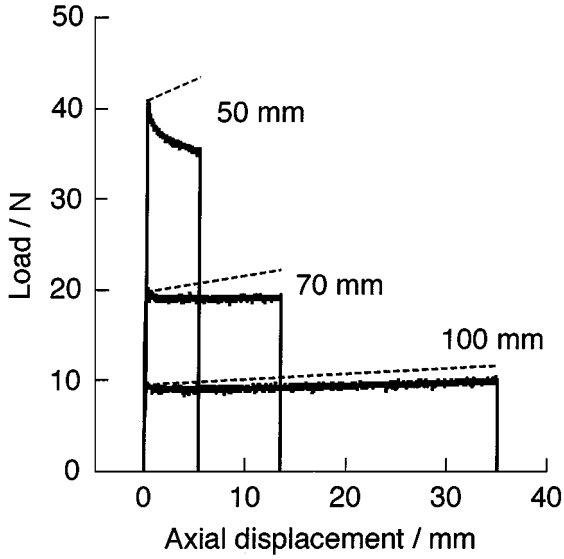

Figure 6 Load-axial displacement diagrams of axial compression bending tests on T4 fiber composite strands. Composite strands are 1.2 mm in diameter and lengths are shown in figure. Experimental results (-) and values calculated with $EI = 4.16 \times 10^{-2}$, 3.96×10^{-2} and 3.91×10^{-2} Nm^2 respectively for $L = 50$, 70 and 100 mm (. . .) are shown.

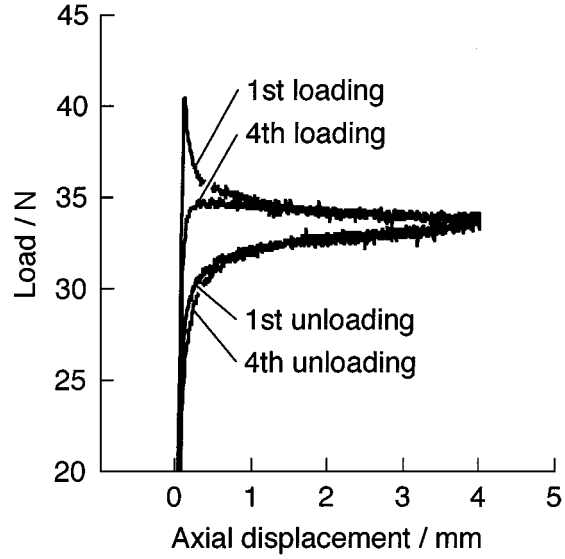

Figure 7 Load-axial displacement diagrams of cyclic axial compression bending tests on T4 fiber composite strand. Composite strand is 50 mm long and 1.2 mm in diameter. Loading and unloading processes of the first and the fourth cycles are shown.

revealed for the carbon film since the film is not perfectly straight and the loading point may be slightly eccentric in the actual tests. The compression curve at later stage, however, follows the prediction of the theory almost exactly.

The compression curves of the T4 fiber composite strands 50, 70 and 100 mm long and 1.2 mm in diameter are shown in Fig. 6. In this figure, the compression curves predicted with $EI = 4.16 \times 10^{-2}$, 3.96×10^{-2} and 3.91×10^{-2} Nm^2 respectively for $L = 50$, 70 and 100 mm are also shown. The compression load is largest for the shortest specimen as is predicted from the theory. The measured compression curves, however, do not follow the prediction of the theory, and the deviation from the theory is largest for the shortest specimen. For the 50 mm long composite strand, the load decreases with increasing axial displacement after the specimen buckled, which is opposite to the theory.

In order to see whether the compression curve for the 50 mm long composite strand is reversible during loading and unloading, cyclic axial compression bending tests were carried out. The compression curves at the first and the fourth cycles are shown in Fig. 7. The rapid decrease in compression load with axial displacement observed for the first loading does not take place during later loading. The compression curve during unloading does not follow the compression curve during loading, and a hysteresis loop is produced. Except for the first loading, the compression curves during loading and those for unloading, respectively, almost coincide. The residual axial displacement after returning the compression load to zero is quite small.

The falling load compression curve and the hysteresis loop appearing in Fig. 7 are not due to the machine strain of the loading instrument. This was confirmed by carrying out cyclic axial compression bending tests on a strip of a carbon tool steel (JIS:SK2) 42 mm long, 8.7 mm wide and 0.38 mm thick. These sizes of the specimen were determined so that the maximum compression load reached was equal to the maximum load for the 50 mm long composite strand. The results are shown in Fig. 8. The load increases with axial displacement and the hysteresis loop is not produced for this test.

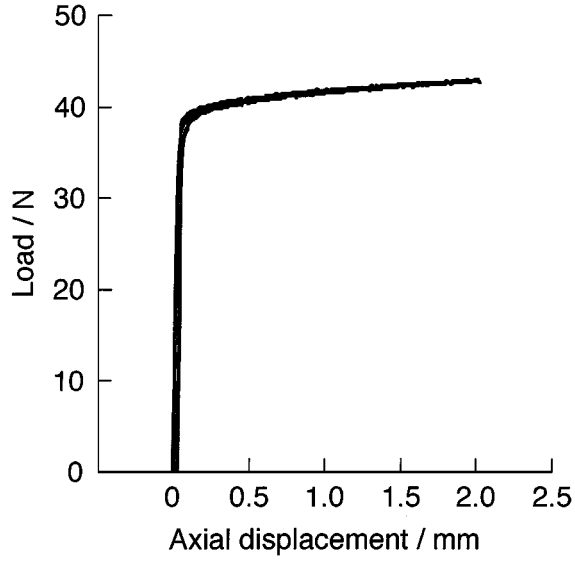

Figure 8 Load-axial displacement diagrams of cyclic axial compression bending tests on strip of carbon tool steel (JIS:SK2). Carbon tool steel is 42 mm long, 8.7 mm wide and 0.38 mm thick. Loading and unloading processes of the first and the third cycles are shown.

It has been known that fabrics when buckled behave in a very different way from the elastic bar, and a falling load compression curve and a hysteresis loop during loading and unloading are produced. This behavior is interpreted in terms of the internal friction between the fibers in the intersection [11]. That is, in order to change the curvature of the fabrics, the applied bending moment should be larger than the frictional couple needed to overcome the internal friction. Thus, a part of the fabric does not change its curvature in a region where the bending moment is smaller than the frictional couple.

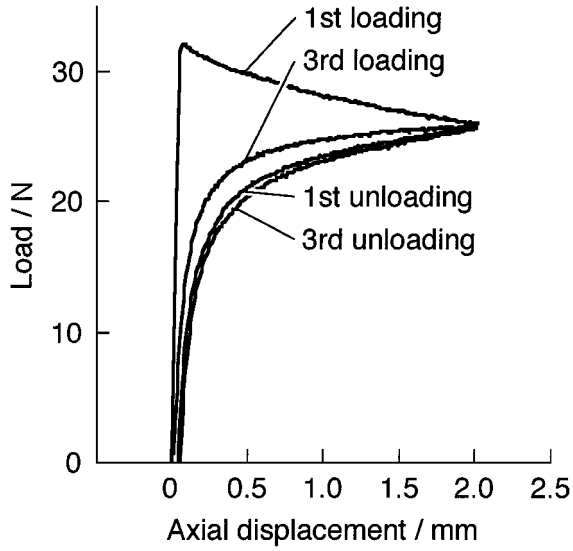

Figure 9 Load-axial displacement diagrams of cyclic axial compression bending tests on stainless steel wire (JIS:SUS304). Stainless steel wire is 50 mm long and 1.0 mm in diameter. Loading and unloading processes of the first and the third cycles are shown.

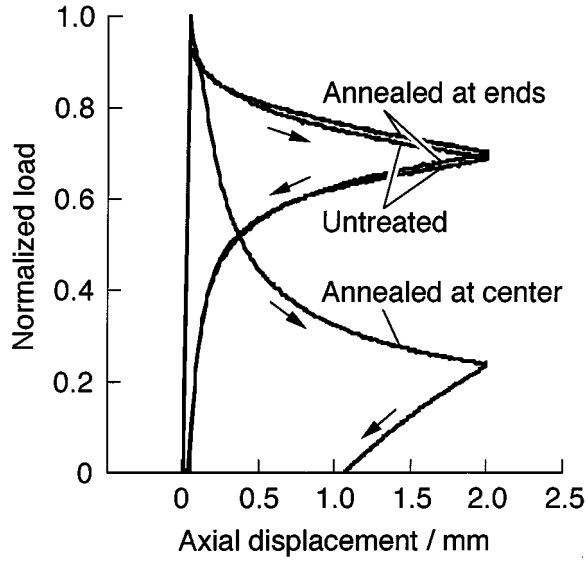

Figure 10 Load-axial displacement diagrams of cyclic axial compression bending tests on stainless streel wires (JIS:SUS304) which were untreated, annealed at both ends and annealed at central portion. Stainless steel wires are 50 mm long and 1.0 mm in diameter. Loading and unloading processes of the first cycle are shown by normalizing loads with maximum values.

This region gradually diminishes with increasing deflection and the load decreases accordingly. A characteristic behavior resulting from the internal friction is that a large axial displacement remains after returning the compression load to zero. For the composite strand, however, the residual axial displacement is quite small. It is unlikely that the internal friction acts in the composite strand in which the bonding between the fibers and the matrix resin is considered to be perfect. Thus, another factor should be considered to interpret the buckling behavior of the 50 mm long composite strand.

If a material is stressed beyond the proportional limit during bending, a falling load compression curve is obtained [5]. The cyclic axial compression bending tests were carried out on a stainless steel wire (JIS:SUS304) 50 mm long and 1.0 mm in diameter. The compression curves of the first and the third cycles are shown in Fig. 9. The compression curves of the stainless steel wire resemble those of the 50 mm long composite strand. Rapid decrease in load during the first loading, almost constant hysteresis loops during later cycles and a small residual axial displacement after returning the compression load to zero are also observed for the stainless steel wire.

The falling load compression curve of the stainless steel wire shown above is not due to a local deformation of the specimen at the loading points. This can be shown by investigating the compression curves of the stainless steel wires which were annealed at the ends of the specimen and at the central portion of the specimen. The normalized compression curves of the untreated and annealed stainless steel wires are compared in Fig. 10. The annealing of the stainless steel wire near the loading points does not cause significant change in the compression curve, while the annealing at the central portion enhances the decrease in the compression load with axial displacements. This indicates that the decrease in the compression load with axial displacement is related to the deformation of the specimen at the central portion.

In the loading process of the axial compression bending tests, an axial compressive stress is imposed on the specimen up to a critical value, and after the specimen buckles, the compressive stress increases at the concave side and decreases at the convex side of the specimen. The rapid decrease in the compression load during the first loading of the stainless steel wire is considered to be due to an inelastic deformation taking place at the concave side of the specimen where the material is stressed beyond the proportional limit. Although the residual axial displacement was small, it was observed that a slight bending of the untreated stainless steel wire remained after returning the compression load to zero. Thus, the shapes of the specimen to which the compression load is applied during the first and later loading differ slightly, leading to different compression curves between the first and later loading. The development of the hysteresis loop suggests that even at equivalent axial displacements, the stress distributions in the specimen differ between loading and unloading.

In the case of the composite strand, the tensile stress-strain relation is almost elastic up to fracture. The shear stress arising in the composite strand at the initial stage of the axial compression bending, where the compression load decreases markedly, is small. Thus, it is considered that the falling load compression curve of the 50 mm long composite strand is due to the inelastic deformation taking place at the concave side of the composite strand similarly to the stainless steel wire. The micro-buckling of the fibers in the concave side of the composite strand is a possible cause of the inelastic deformation. Although this micro-buckling is not obviously observed for the resin system used in this study, a composite strand fabricated with a matrix resin containing a large amount of difunctional diluent showed a wavy surface at the convex side of the specimen during the axial compression bending.

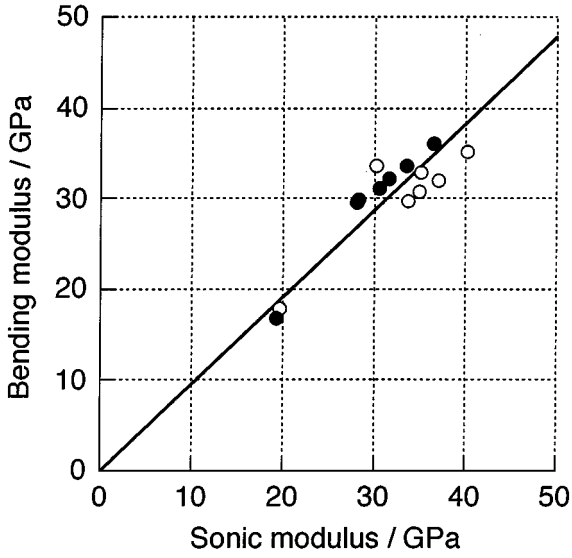

Figure 11 Bending modulus plotted against sonic modulus for PCDI-based carbon films. Films are 50 mm long, 150 (○) and 250 (●) μm thick and processed at various temperatures. Regression line with a slope of 0.96 is shown.

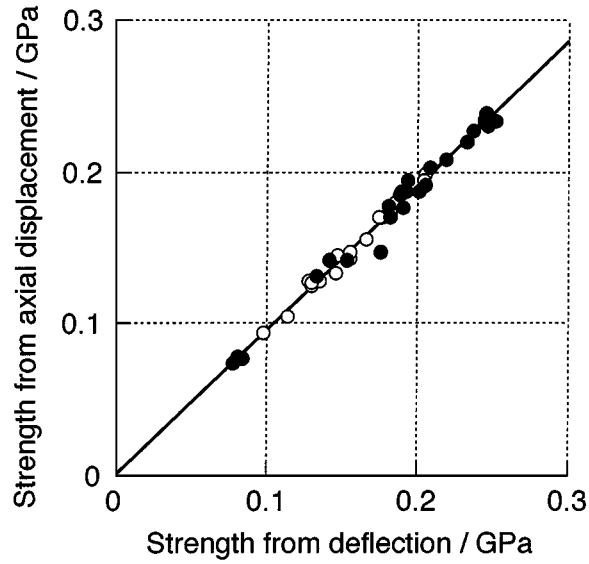

Figure 12 Bending strength estimated from axial displacement plotted against that estimated from deflection for PCDI-based carbon films. Films are 50 mm long, 150 (○) and 250 (●) μm thick and processed at various temperatures. Regression line with a slope of 0.95 is shown.

4.2. Estimation of bending modulus

For the ideal axial compression bending test of a perfectly straight bar, the critical load at which the bar buckles can be determined accurately, and the bending modulus is calculated by using Equation 5. The carbon films, however, start to bend gradually as shown in Fig. 5. Thus, the bending modulus of the carbon films was calculated by using the compression load which was obtained by linearly extrapolating the compression curve at later stage to zero axial displacement. Thus determined bending moduli for the 50 mm long carbon films with different thicknesses and processing temperatures are compared with sonic moduli in Fig. 11. The bending modulus almost coincides with the sonic modulus.

4.3. Estimation of bending strength

With the present experiments, there are two methods to estimate the bending strength. The first method is to use the measured deflection directly as the value of δ_t in Equation 17. The second method is to obtain the value of δ_t in Equation 17 from the measured axial displacement δ_a by using Equations 13 and 14. The strengths estimated by using these two methods are compared in Fig. 12 for the carbon films with different thicknesses and processing temperatures. No marked difference was found in the results of these two methods.

If the specimen shows a falling load compression curve as is observed for the 50 mm long composite strand, using Equation 17 in the estimation of the bending strength is inaccurate. An inexact but practically acceptable way to estimate the bending strength for such specimens is to treat the inelastic deformation of a part of the specimen as a decrease in the effective cross-section size of the specimen. The effective cross-section size is determined by using the modulus of the specimen as follows: From the deflection δ_t or the axial displacement δ_a at fracture, the value of p is calculated by using Equations 14 or 13, and the value of k by using Equation 6. If the modulus E is known, the effective moment of inertia of area I is calculated by using Equation 4 with the compression load at fracture, and the effective thickness t is obtained by using Equation 18 or 20 according to the shape of the cross-section. With these values of I and t, the bending strength σ_b is calculated by using Equation 17. As to the value of the deflection δ_t in Equation 17, either the directly measured value or the value calculated from the axial displacement δ_a can be used.

The method shown above is preferable even in the case where the specimen shows a normal compression curve in order to minimize error in the bending strength caused by the error in the measurement of the cross-section size. The variation in the calculated values of the bending strength with the variation in the cross-section diameter is demonstrated in Fig. 13. The

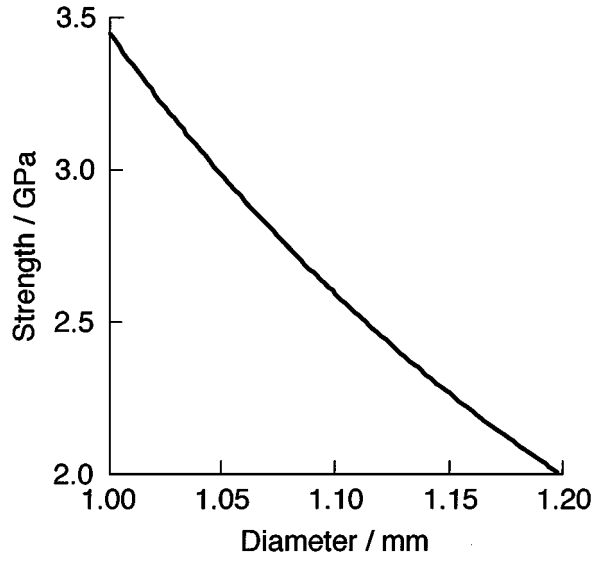

Figure 13 Bending strength of T4 fiber composite strand plotted against cross-section diameter used for calculation. Composite strand is 100 mm long and fractured at compression load of 9.4 N and deflection of 36 mm.

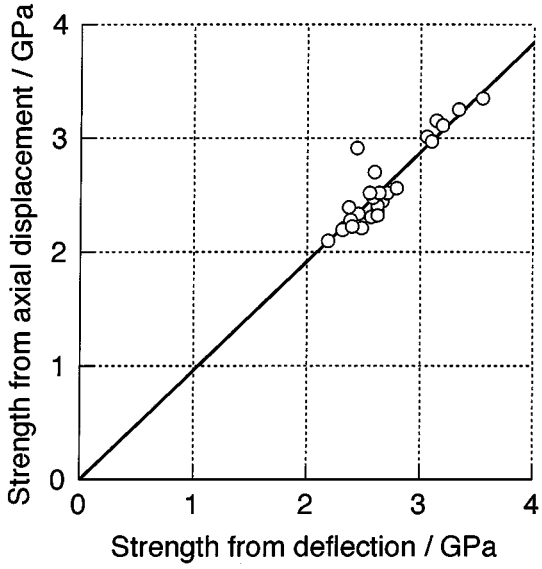

Figure 14 Bending strength estimated from axial displacement plotted against that estimated from deflection for T4 fiber composite strands. Composite strands are 50, 70 and 100 mm long with different cross-section diameters. Regression line with a slope of 0.96 is shown.

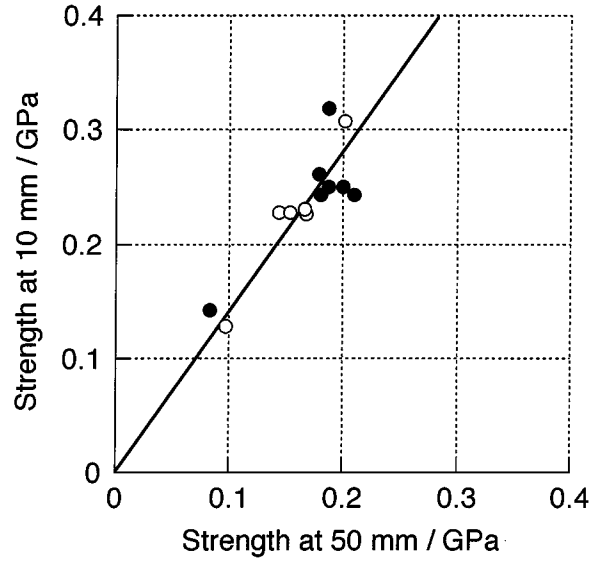

Figure 15 Bending strength of 10 mm long specimen plotted against that of 50 mm long specimen for PCDI-based carbon films. Films are 150 (○) and 250 (●) μm thick and processed at various temperatures. Regression line with a slope of 1.4 is shown.

bending strength in this figure was calculated for the T4 fiber 100 mm long composite strand with a fracture load of 9.4 N and a deflection at fracture of 36 mm. By considering fluctuation of the cross-section diameter and deviation of the shape of the cross-section from the circle for the actual composite strands, a relatively large error would be involved in the bending strength if it was calculated from the measured value of the cross-section diameter.

T4 fiber 50, 70 and 100 mm long composite strands having different cross-section diameters were prepared by using single fiber tows and dies with different diameters. The bending strengths of these specimens were estimated by calculating the effective cross-section diameters from the sonic modulus and the deflection or the axial displacement. The bending strengths estimated from the axial displacement are compared with those estimated from the deflection in Fig. 14. The difference in the bending strengths estimated with these two methods is small. From the experimental view point, the measurement of the axial displacement is easier than the measurement of the deflection. Thus, in the following, the values of the bending strength of the carbon films and the composite strands, estimated from the axial displacement will be shown.

4.4. Bending modulus and strength of carbon films

The dependence of the bending strength on the specimen length is demonstrated in Fig. 15 for the PCDI-based carbon films with different thicknesses and processing temperatures. A higher strength is obtained for the shorter specimens, while the strength values at these two different lengths are in proportion. This can be attributed to the size effect of the strength of the carbon films due to stochastic nature of the existence of critical flaws, and the changes in the effective specimen length with the length of the specimen tested as shown in Section 2.2.

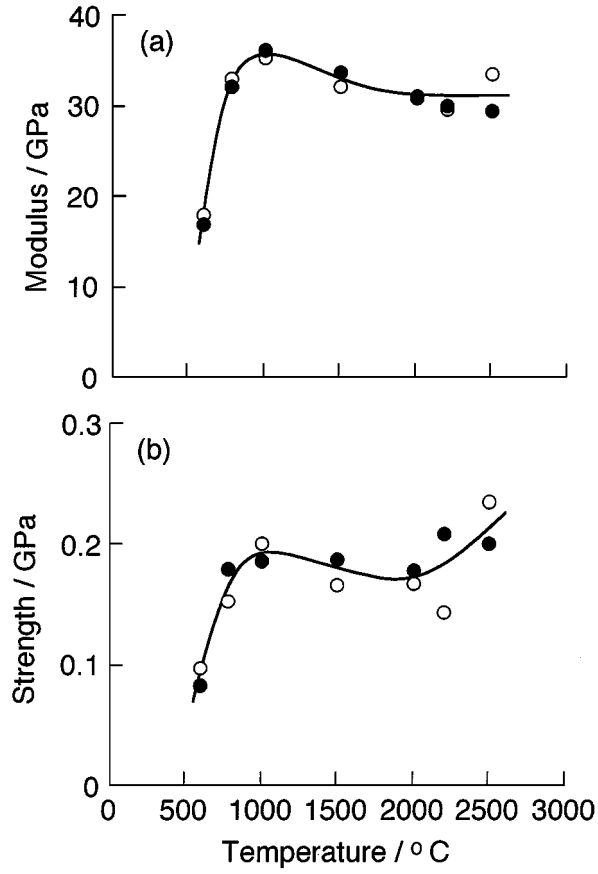

Figure 16 Bending modulus (a) and bending strength (b) plotted against processing temperature for PCDI-based carbon films. Films are 50 mm long and 150 (○) and 250 (●) μm thick.

The bending modulus and the bending strength of the 50 mm long PCDI-based carbon films are plotted against the processing temperature in Fig. 16. The bending strength and modulus increase with processing temperature up to about 800 °C. It was observed that the fracture of the carbon films by the axial compression bending initiated at the tensile side of the films.

TABLE II Modulus and results of axial compression bending tests on composite strands

Fiber	Length (mm)	Diameter (mm)	Fiber volume fraction	Sonic modulus (GPa)	Compression load at fracture (N)	Axial displacement at fracture (mm)
T4	50				31.7	5.70
	70	1.2	0.42	99.6	17.5	13.6
	100				9.2	40.6
	50				24.4	7.65
	70	1.0	0.55	141	13.1	19.4
	100				7.4	47.5
H4	50	1.0	0.42	168	29.6	1.47
X5	50	1.2	0.50	305	48.5	0.52

TABLE III Bending strength and fracture mode of composite strands

Fiber	Length (mm)	Diameter (mm)	Effective diameter (mm)	Bending strength (GPa)	Reduced bending strength (GPa)	Fracture mode
T4	50		1.1	2.4 ± 0.13	5.7	Tensile
	70	1.2	1.1	2.3 ± 0.15	5.5	
	100		1.1	2.5 ± 0.26	5.9	
	50		0.96	3.4 ± 0.08	6.1	
	70	1.0	0.95	3.3 ± 0.17	6.0	
	100		0.95	3.2 ± 0.15	5.8	
H4	50	1.0	0.98	1.8 ± 0.05	4.2	Compressive
X5	50	1.2	0.95	1.9 ± 0.10	3.7	Tensile

The development of the structure of these films during heat-treatment has been reported in another paper [8].

4.5. Bending strength of composite srands

The bending strengths of T4, H4 and X5 fiber composite strands were estimated by calculating the effective cross-section diameters. The experimental data and the results of calculation are summarized in Tables II and III. The reduced bending strength shown in Table III is the strength per unit cross-section area of fibers, which was calculated by dividing the bending strength with the fiber volume fraction. The variation of the reduced bending strength with cross-section diameter and specimen length is small. This suggests that the bending strength of the specimens showing falling load compression curves can be practically estimated by using the effective cross-section diameter at fracture. The effective cross-section diameters are smaller than the initial cross-section diameters also for the 70 and 100 mm long composite strands. This is because even for longer composite strands, the slope of the compression curve is smaller than the prediction of the theory as is shown in Fig. 6. It is also known that the length dependence of the strength of the composite strand is smaller than that of the carbon films in the length region tested.

The fracture of the H4 fiber composite strands initiated from the compressive side of the specimen. On the other hand, the fracture of the T4 fiber composite strands initiated from the tensile side of the specimen. This was judged from the observation of the fracture process and the optical microscopy of the longitudinal cross-section of a specimen to which a compression load just before fracture had been applied. That is, in the longitudinal cross-section, fiber breakage was observed only at the convex side of the specimen. For the X5 fiber composite strands, definite determination of the fracture mode from the observation of the fracture process was difficult, though it seemed to be a tensile fracture judging from the fracture surface. The scanning electron micrographs of H4, T4 and X5 fiber composite strands after axial compression bending tests are shown in Fig. 17.

It is known from comparison between the reduced bending strength shown in Table III with the tensile or compressive strength, corresponding to the fracture mode, of the fibers shown in Table I that the reduced strength is larger than the strength of the component fibers. This is presumably because the composite strands do not fracture catastrophically at the moment when the maximum stress near surface of the composite strands locally reaches the critical values.

The maximum values of the shear stress which arise in the composite strands at fracture were calculated using Equation 28. Among the composite strands shown in Table I, the maximum shear stress is the largest for the T4 fiber 50 mm long composite strand with a diameter of 1.0 mm and is calculated to be 32.1 MPa. The smallest value is for the T4 fiber 100 mm long composite strand with a diameter of 1.2 mm and is calculated to be 12.5 MPa. Since the interfacial shear strength between this fiber and the epoxy resin estimated with a fragmentation test is 45.3 MPa [12], it is known that the interfacial shear fracture did not take place during the axial compression bending tests on the composite strands shwon in Table I.

5. Conclusions

The bending strength estimated from the axial displacement and the compression load coincided with the bending strength estimated from the deflection and the compression load for both carbon films and carbon fiber composite strands.

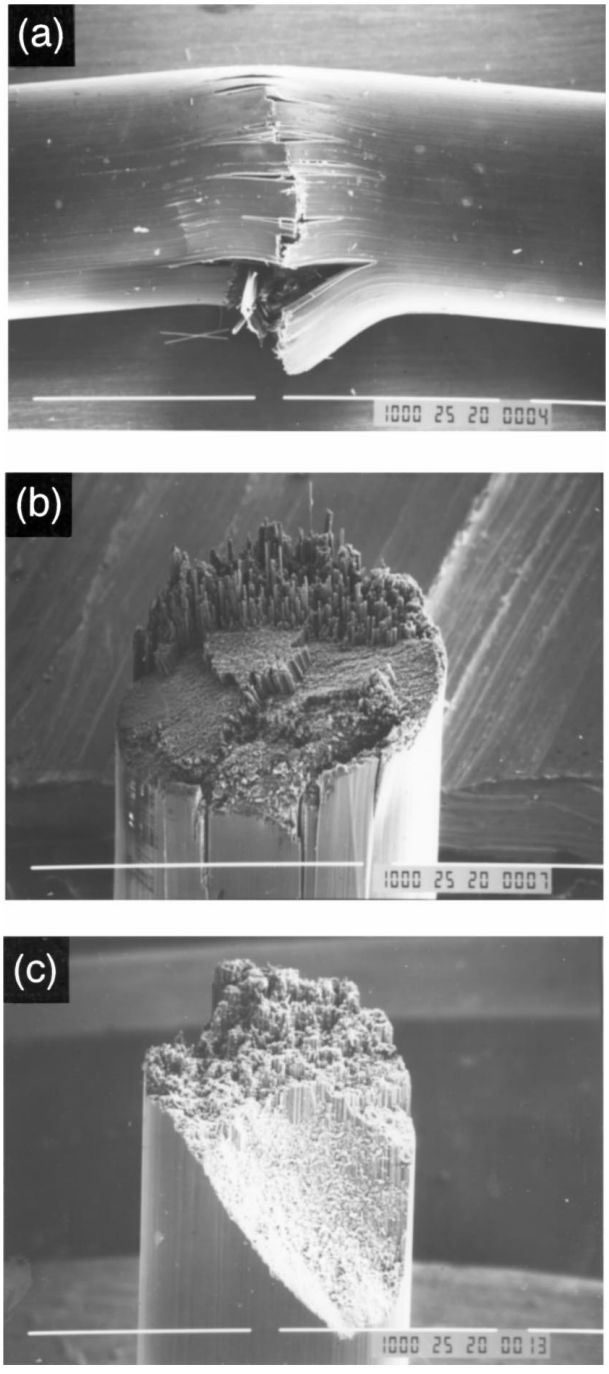

Figure 17 Scanning electron micrographs of H4 (a), T4 (b) and X5 (c) fiber composite strands after axial compression bending tests.

For the carbon films, the bending strength depended on the specimen length due to stochastic nature of the existence of critical flaws. The effective specimen length was calculated as a function of the length of the specimen tested. The bending modulus of the carbon films estimated from the compression load at which specimens buckled coincided with the sonic modulus.

For the carbon fiber 50 mm long composite strand, the compression load decreased with increasing axial displacement. The compression curve of this composite strand was not reversible during loading and unloading, and a hysteresis loop was produced. Similar compression curves were also obtained for the cyclic axial compression bending tests on a stainless steel wire. The bending strength of the specimens showing falling load compression curves can be practically estimated by using the effective cross-section sizes at fracture. This analysis method is also preferable in order to minimize the error in the bending strength caused by the error in the measurement of the cross-section size. The analysis of the shear stress showed that interfacial shear fracture did not take place during the axial compression bending tests on the composite strands. The reduced bending strengths estimated with the axial compression bending tests were larger than the strengths of the component fibers determined with the tensile and micro-compression tests.

References

1. H. IWAI, M. UEMURA and T. HAYASHI, *J. Jpn. Soc. Comp. Mater*. **18** (1992) 60.
2. H. IWAI, M. UEMURA and S. UEMURA, *ibid.* **20** (1994) 62.
3. H. FUKUDA, *J. Jpn. Soc. Aeronautical and Space Sci.* **41** (1993) 482.
4. B. LAUKE and K. FRIEDRICH, *Composites Manufacturing* **4** (1993) 93.
5. S. TIMOSHENKO and J. M. GERE, "Theory of Elastic Stability," 2nd ed. (McGraw-Hill, New York, 1961) pp. 76–82.
6. S. TIMOSHENKO, "Strength of Materials, Part I: Elementary Theory and Problems," 3rd ed. (Van Nostrand Reinhold Company, New York, 1958) p. 120.
7. S. MAEDA, T. HASHIMOTO, A. TAKAKU, A. HAGIWARA, K. SAITO and T. SUZUKI, *Tanso* **168** (1995) 149.
8. M. SHIOYA, M. NAKATANI, H. KITANO, A. TAKAKU, Y. ARAKI, Y. TAKAHASHI and T. SUZUKI, *Carbon* **34** (1996) 1229.
9. M. NAKATANI, M. SHIOYA and J. YAMASHITA, *ibid.* accepted.
10. E. HAYAKAWA, M. SHIOYA and A. TAKAKU, *Adv. Composite Mater.* **4** (1994) 33.
11. J. HEARLE, P. GROSBERG and S. BACKER, "Structural Mechanics of Fiber, Yarns, and Fabrics" (Wiley-Interscience, New York, 1968) pp. 355–369.
12. M. SHIOYA, S. YASUI and A. TAKAKU, *Composite Interfaces* **4** (1997) 379.

Received 26 August 1997
and accepted 15 October 1998